The Applicability of Lumped Wheel Models in the Analysis of Dynamic Wheel-Rail Contact for Short-Length Rail Irregularities

MICHAËL J.M.M. STEENBERGEN[1]

Railway Engineering, Delft University of Technology, the Netherlands

SUMMARY

A classification of wheel-rail contact is given. Difference is made between modelling of a running wheel with continuous single-point contact, as is common practice in wheel-rail contact analysis, and a wheel with transient double-point contact, which may occur for rail irregularities with curvatures larger than that of the wheel circumference. It is shown that application of the first model for these irregularities will strongly underestimate the contact forces as it does not describe occurring mechanisms correctly. Further it is shown that in principle it is not possible to describe the second type of contact fully correct with a lumped wheel model. Both wheel models are formulated mathematically for some basic contact cases. Afterwards, results are applied to a linear track model. Analytical closed-form solutions are found in the frequency domain for arbitrary type of contact and numerically transformed to the time domain.

Keywords: rail joint, dipped joint, wheel-rail contact, wheel model, impact load

2000 Mathematics Subject Classifications: 70B10, 70E55, 70G99, 70J50, 74H05, 74H15

Title in running head: Modelling of Wheels and Rail Discontinuities in Wheel-Rail Contact Analysis

NOMENCLATURE

A	cross-sectional area of a rail
E	Young's modulus of steel
F	contact force wheel-rail
i	imaginary unit

[1] Delft University of Technology, Faculty of Civil Engineering and Geosciences, Department of Road and Railway Engineering (VBK), P.O. Box 5048, NL 2600 GA Delft. Tel: + 31 (0)15-27 81759. Fax: + 31 (0)15-27 83443. Email: M.J.M.M.Steenbergen@citg.tudelft.nl

k_H Hertzian contact stiffness wheel-rail

k_f foundation stiffness of an embedded rail

k_{susp} stiffness of the primary wheel suspension corresponding to one wheel

I moment of inertia of the rail cross-section

m_w mass of a train wheel (half unsprung mass)

M train wheel centre

Q static wheel-load

R train wheel radius

R_{rail} railhead radius

s Laplace parameter, defined as $s = \sigma + i\omega$ with σ some small positive value and ω the frequency

t time

u vertical degree of freedom of the lumped wheel-mass

u_0 step height in the vertical rail-geometry

u_1 total height difference in the vertical rail geometry for a multi-linear vertical rail-geometry

v train velocity

v_0 initial velocity of the train wheel-mass

w vertical degree of freedom of the rail

x longitudinal coordinate of the rail-geometry

z vertical height of the rail-geometry

γ relative angle in the vertical rail-geometry

ρ steel density

υ Poisson's ratio of steel

1. INTRODUCTION

In the analysis of wheel-rail contact, several modelling methods are applied. In general, difference can be made between mixed discrete-continuous descriptions and finite element models. The first type of models

describes each discrete element (track and vehicle components) by its equation of motion. The complete set of coupled equations then is solved analytically in the frequency domain, or with a time-stepping routine in the time domain.

In this type of models as well as in several finite element models, the train wheel is commonly modelled as a lumped mass connected to a vertical Hertz spring, mostly non-linear, representing the wheel-rail contact stiffness [1, 2 *et al.*]. Also e.g. the software package ADAMS/Rail works like this [3].

A problem arises when the wheel-rail contact has a spatial discontinuity. Such discontinuity may occur e.g. for dipped joints, insulated rail joints (IRJ), bolted rail joints where both so-called fishplates have a smaller vertical bending stiffness than the rail itself, crossings, where apart from a gap the transition from the wing rail to the crossing nose often has a difference in height, and even in the case of badly welded connections in continuously welded track (CWR).

Fig. 1. Examples of IRJ's. Left: the wear pattern shows the occurrence of additional bending through impact at the joint.

In 1974 Jenkins, Lyon and others (British Rail) presumably were the first to study wheel-rail contact for a dipped joint in their well-known paper [1] where they present approximating formulae for determining $P1$ and $P2$ forces. They use a vertical non-linear Hertz spring for modelling the contact wheel-rail. However, they don't consider the possibility of a discontinuity in the contact at the dip.

In more recent literature, some attention has been paid to this problem or some specific aspect of it.

Andersson and Dahlberg [4] analyse wheel-rail contact for crossings with a certain gap between wing rail and nose (without height difference), applying a non-linear Hertzian spring in modelling the contact. They use a finite element model for the turnout. For the gap a fictitious beam element is used, trough-shaped between the

two end-nodes of adjacent elements of the rail. Thus discontinuities in vertical wheel displacement and its time-derivatives are avoided. Increases in contact force are found up to 100% at 70 km/h and 200% at 150 km/h as compared to the static value. The dynamic amplification occurs due to two reasons: not only the geometrical discontinuity is playing a role, but also the sudden change in track flexibility when the wheel moves from the wing rail to the nose rail.

Dukkipati and Dong [5] study the problem of a dipped rail-joint. However, the wheel-rail contact is modelled a multi-spring-contact (partly continuous contact), so that a spatial contact discontinuity cannot occur.

Chen and Kuang [6] study the contact stress variation near insulated rail joints. They use a finite element model for both wheel and rail. Results show that the Hertzian contact theory is no longer able to predict the contact stress distributions around the rail joints. In a following study by Chen [7] elastoplastic finite elements are used for the same analysis. It is found that serious plastic deformations may occur at the rail ends.

Wu en Thompson [8] study impact noise due to a wheel passing over rail joints. A linear model for wheel-rail impact at a joint in the time domain is presented and wheel centre trajectories for dipped joints are used as model input. For a joint with a gap of 7 mm and a step-up of 1 mm dynamic load amplifications are found of 400% and 600% for speeds of 80 and 160 km/h respectively.

Wu and Thompson [9] study the effects of track non-linearity on wheel-rail impact which may occur due to wheel and rail discontinuities. Only the case of a wheel flat is considered, and the wheel-rail contact has no spatial discontinuity.

Schupp, Weidemann and Mauer [10] simulate the contact between wheel and rail for a railway vehicle running through a switch with multibody system simulation. Main focus is on the changing rail profile and no specific attention is paid to the rail discontinuity.

Koro, Abe, Ishida and Suzuki [11] pay attention to the problem of more-point-contact between wheel and rail, occurring for discontinuous rail with bolted joints with certain gap. They developed a finite element model for wheel-rail contact, applying the Hertzian spring, and use a modified constitutive relation of the Hertzian contact model, introduced in [12], with changing parameters in the vicinity of rail edges. This way they smoothly change the single-point-contact state to a two-point-contact stage and avoid a discontinuity in the contact. With the developed model they investigate the influence of the train speed and the gap size on the

impulsive contact force excited by wheel passage on a rail joint. They find excited loads which are much higher than those occurring for a wheel running on a continuous railhead.

In all mentioned studies, except for [8], the spatial discontinuity in wheel-rail contact is avoided where the Hertzian spring model is used. This paper is mainly devoted to the applicability of lumped wheel models for the different types of short-length rail irregularities, with emphasis on those irregularities where a spatial discontinuity in wheel-rail contact occurs.

2. CLASSIFICATION OF WHEEL-RAIL CONTACT

A perfectly circular wheel running on a perfectly straight rail continuously has a single contact-point in time. The contact is a real point when the elasticity of both elements is not taken into consideration, in a purely geometrical approach. As soon as any irregularity occurs in the vertical rail profile, this may change into a double-point-contact, or even a more-point-contact or partly continuous contact. This second type of contact can only occur for irregularities with a length-scale smaller than the wheel radius, or when the positive curvature of the vertical rail geometry exceeds the curvature of the wheel rim.

If this type of contact is transient, as it is for a running vehicle, it will cause a development of the wheel-rail contact force which will be completely different from that which occurs in the case of a single-point-contact which is continuous in time.

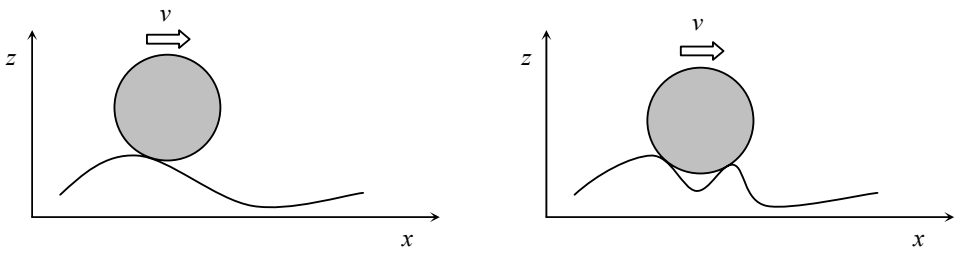

Fig. 2. Types of wheel-rail contact; continuous single-point contact (left) and transient double-point contact (right)

Both types of contact will be analysed separately in the following as well as their dynamic modelling. This will be done first for a wheel running on a completely rigid rail and foundation. Attention then can be focused completely on the modelling of the wheel. Later on also rail and track modelling will be included (section 6).

3. CONTINUOUS SINGLE-POINT CONTACT

If wheel and rail have a continuous single-point-contact, the wheel may be modelled in multi-body-dynamics as a lumped mass, with all mass concentrated in the gravity centre, supported by a spring, representing the radial wheel stiffness or the Hertzian wheel-rail contact stiffness. This stiffness is non-linear, but may be linearised in a simplistic approach for small deviations round a certain load-level. As long as single-point contact is present, any irregularity in the vertical rail surface can be modelled as an excitation of the contact-point wheel-rail, or the contact-point between the Hertzian spring and the rail. For a wheel on rigid rail with height $z(x)$ the corresponding formulation of the wheel on the Hertzian spring becomes that of a simple oscillator (Figure 3, $x = vt$):

$$m_w \ddot{u}(t) + k_H u(t) = k_H z(t) \tag{1}$$

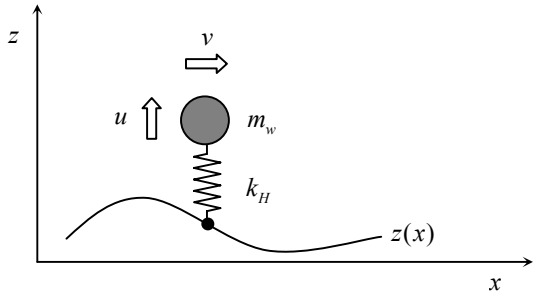

Fig. 3. Wheel modelling for continuous single-point contact wheel-rail

Application of this wheel-model (with linear or non-linear Hertzian spring) is common practice in the analysis of wheel-rail contact, as stated in the introduction.

4. TRANSIENT DOUBLE-POINT CONTACT

The double-point contact will be considered first for a most basic case: the train wheel passes an upward step in the vertical rail geometry. For this case the basic mechanisms playing a role are most easy to analyse. Afterwards, a more complex case will be treated. In this section only kinematical or geometrical derivations are given, which means inertia is not accounted for, and both wheel and rail are considered infinitely rigid. Some implications will be discussed in section 5.

4.1. Step in the vertical rail geometry

The considered case is shown in Figure 4, where also some notations are introduced. The wheel radius is denoted by R and its centre by M; the step height is u_0 and the velocity v.

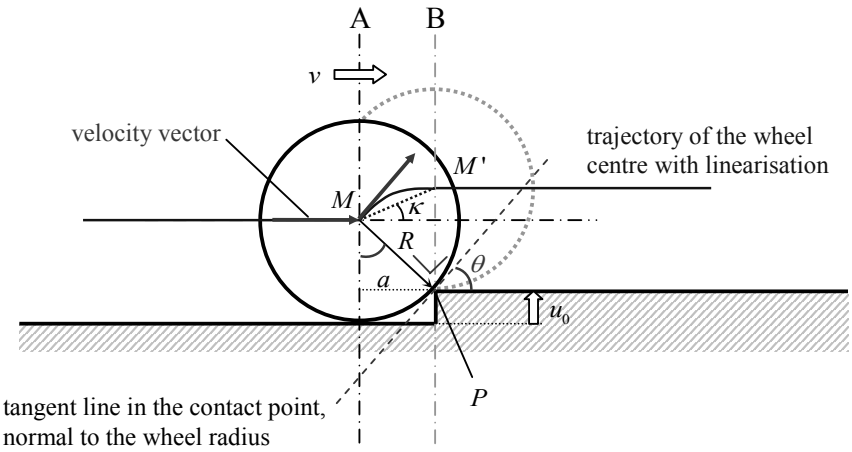

Fig. 4. Kinematical wheel displacement for a vertical step in the rail surface; $u_0 \le R$

The vertical displacement of the wheel centre is not described by the step function, due to its non-zero radius. In Figure 3 the trajectory of the wheel centre is shown; it consists of two straight lines, connected by a circle segment. The circle segment has centre P (the instantaneous centre of rotation when moving from position A to B) and radius R. The rolling wheel has continuous single-point-contact with the rail, except for position A, where a two-point-contact occurs, immediately followed by a shift of the contact-point in circumferential direction of the wheel. This two-point-contact at position A causes a discontinuity in the first spatial derivative of the trajectory. In the time domain (transformation via the linear operator v, the train velocity), this implies a discontinuity in the velocity (time-derivative of the displacement) at position A. The result is an instantaneous change in the upward wheel-mass velocity, or an impact contact-force, as the duration of the velocity change is zero. This also implies that the magnitude of the contact force during impact is undetermined. The instantaneous velocity change is also shown in Figure 4; arriving in position A the velocity vector is horizontal, leaving this position its direction is parallel to the tangent line at the wheel in P, as its orientation is always normal to the wheel radius towards the contact-point.

As was done for the continuous single-point contact, the double-point contact now will be formulated mathematically for the wheel-model of Figure 3. Assuming the time moment of reaching position A as $t = 0$, the initial vertical velocity of the wheel mass reads:

$$\dot{u}(0) = v \cdot \sin\theta = v \cdot \sqrt{\frac{2u_0}{R}} \tag{2}$$

The momentaneous double-point-contact is followed by single-point contact again, which means the subsequent vertical excitation of the wheel mass can be modelled as an excitation at the base of the Hertz spring, as discussed before. This spring base displacement is equal to the change in vertical distance between the wheel centre trajectory and the vertical rail surface. Here, the displacement function is linearised (taken is the chord of the circle segment, the dotted line in Figure 4), to keep expressions simple. The excitation is shown in Figure 5 as a function of time.

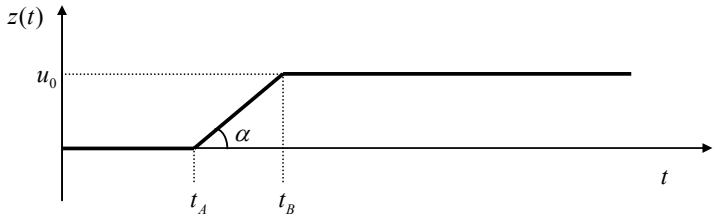

Fig. 5. Linearised trajectory of the wheel centre versus time for a step in the rail surface

The above now will be written in formula. For $u_0 \le R$ the following geometric relation holds (compare Figure 4):

$a = \sqrt{u_0(2R - u_0)}$, which is simplified as $\sqrt{2Ru_0}$ for $u_0 \ll R$. (3)

Assuming again $t_A = 0$, the vertical displacement of the spring base in space reads, for $0 < x < a$ with $x = 0$ coinciding with position A:

$$z(t) = \frac{u_0}{a} \cdot x = \sqrt{\frac{u_0}{2R}} \cdot x \tag{4}$$

Assuming a constant train velocity and using $x = v \cdot t$, in the time domain this can be written as:

$$z(t) = \sqrt{\frac{u_0}{2R}} \cdot v \cdot t \tag{5}$$

The displacement function of the Hertz spring base (Figure 5) may be written, in continuous form, for the whole time domain $t \geq 0$, as:

$$z(t) = \frac{u_0}{t_B} t \cdot H(t_B - t) + u_0 H(t - t_B) \tag{6}$$

where H represents the Heaviside-function and t_B is given by:

$$t_B = \frac{\sqrt{2Ru_0}}{v} \tag{7}$$

Substituting (7) into (6), the final displacement function reads:

$$z(t) = \sqrt{\frac{u_0}{2R}} \cdot vt \cdot H\left(\frac{\sqrt{2Ru_0}}{v} - t\right) + u_0 \cdot H\left(t - \frac{\sqrt{2Ru_0}}{v}\right) \quad (t \geq 0) \tag{8}$$

4.2. Multi-linear vertical rail geometry

Now the somewhat more complex case of a piece-wise linear vertical rail surface (a ramp) will be considered (Figure 6).

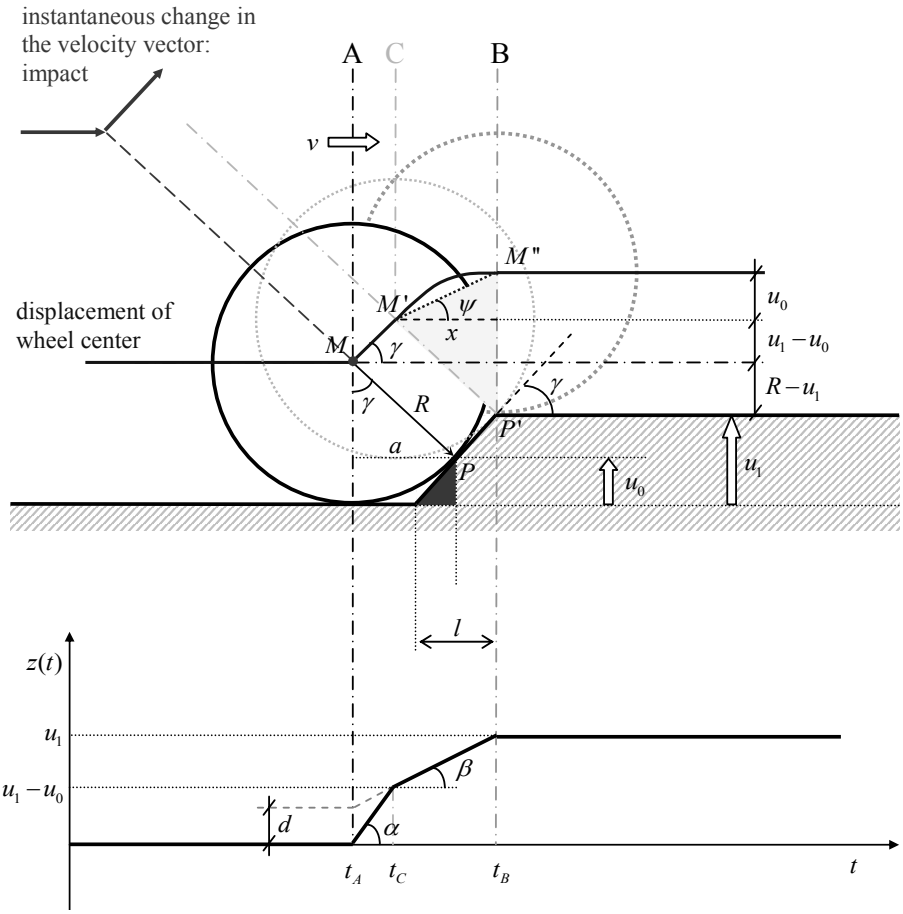

Fig. 6. Derivation of the wheel-model excitation for a multi-linear rail profile (ramp, dipped joint) for $u_1 \le R$

It can be seen immediately that a fictitious step with magnitude u_0 is present; the shape of the hatched (massive) area has no influence. Before discussing this case, a restriction on the applicability of the model of Figure 6 is derived; compare Figure 7. In this figure the situation is shown in which the positions A and C in Figure 6 coincide; the linear part in the displacement MM' (Figure 6) disappears and the situation is reduced to a simple step (with $u_1 = u_0$), as in the model of Figure 7 (the shape of the massive area has no influence). This poses the following restriction on the combination of γ, R and u_1 for which the model of Figure 6 is valid: $u_0 < u_1$ or: $u_1 > R(1-\cos\gamma)$.

Thus, the following validity domains for application of the models of Figure 4 and 6:

- $0 < u_1 < R(1-\cos\gamma)$: step model, with $u_1 = u_0$ (9)
- $R(1-\cos\gamma) < u_1 < R$: multi-linear model

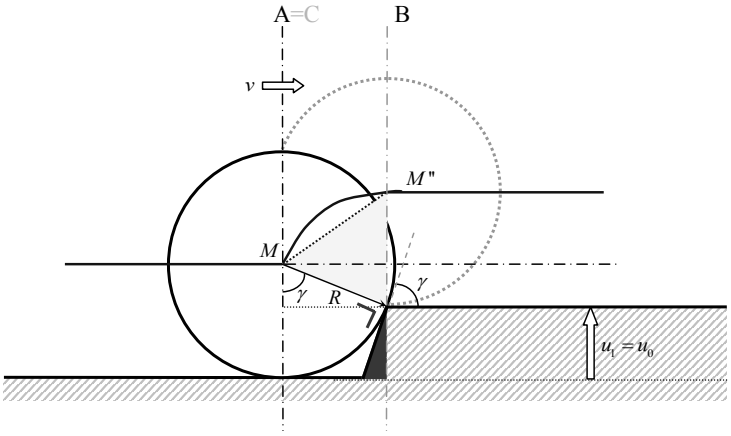

Fig. 7. Transition between step and multi-linear model

In Figure 6 (top) the trajectory of the wheel centre is shown. It consists of two straight lines (before position A and after position B), connected by the linear line segment MM' and the circle segment $M'M''$. A discontinuity in the first derivative (both space- and time-derivative) or an instantaneous velocity change of the wheel mass occurs at position A, where a two-point-contact occurs, immediately followed by a shift of the contact-point in circumferential direction of the wheel, causing an impact. The impact is followed by continuous single-point-contact, and can be described by a displacement at the base of the Hertz spring (Figure 6, bottom). This displacement consists of the straight line segment MM', where the base of the Hertz spring moves from P to P', followed by the circular segment $M'M''$, where the base of the Hertz spring stays in P', but the wheel centre moves from M' to M''. During this movement the vertical distance between the wheel centre and centre of rotation P' changes, which can be considered as a displacement at the base of the Hertz spring. In order to keep expressions simple, this displacement is linearised again, taking the chord of the circle segment (Figure 6, dotted line).

The above now will be written in formula. The time moment t_A is chosen again as $t_A = 0$. For the initial velocity $\dot{u}(0)$ of the wheel mass can be written:

$$v_0 = v \cdot \sin\gamma \tag{10}$$

where γ denotes the slope of the ramp. The following general expression holds for the vertical displacement of the Hertz spring base (compare Figure 6, bottom), for the whole time domain $t \geq 0$ (with $0 \leq t_C \leq t_B$):

$$z(t) = \alpha t \cdot H(t_C - t) + (\beta t + d) \cdot \left(H(t - t_C) - H(t - t_B)\right) + u_1 \cdot H(t - t_B) \tag{11}$$

The slope coefficients α and β are derived in the following. First, the time durations of passing from position A to C (t_{AC}) and from C to B (t_{CB}) are determined.

$$t_{AC} = \frac{MM'}{v \cdot \cos\gamma} \tag{12}$$

The rail inclination γ is defined by $\tan\gamma = u_1 / l$. In the above expression for t_{AC} , the denominator may not be approximated by v since $0 < \gamma < 90^0 \Rightarrow 0 < \cos\gamma < 1$. In the same way, the distance MM' may not be replaced by its horizontal component.

$$t_{AC} = \frac{(u_1 - u_0)/\sin\gamma}{v \cdot \cos\gamma} = \frac{2}{\sin(2\gamma)} \frac{(u_1 - u_0)}{v} \tag{13}$$

The time duration of passing from C to B is given by:

$$t_{CB} = \frac{M'M''}{v \cdot \cos\psi} \tag{14}$$

In contrast to the expression for t_{AC} , in this expression the denominator may be approximated by v , as shown in the relations below:

$$\begin{aligned} &\cos\psi = \frac{x}{M'M''} \\ &x = \sqrt{R^2 - (R-u_0)^2} = \sqrt{2Ru_0 - u_0^2} \approx \sqrt{2Ru_0} \\ &M'M'' = \sqrt{x^2 + u_0^2} = \sqrt{2Ru_0 + u_0^2} \approx \sqrt{2Ru_0} \end{aligned} \tag{15}$$

With $u_0 \ll R$ the term u_0^2 is third-order and will be neglected, or $\cos\psi \approx 1$. Thus, for t_{CB} may be written:

$$t_{CB} = \frac{\sqrt{2Ru_0}}{v} \tag{16}$$

which is the same result as obtained in equation (7) for the step, as expected. The coefficients α and β now follow from:

$$\alpha = \frac{u_1 - u_0}{t_{AC}} = \tfrac{1}{2}\sin(2\gamma) \cdot v \tag{17}$$

and

$$\beta = \frac{u_0}{t_{CB}} = \sqrt{\frac{u_0}{2R}} \cdot v \tag{18}$$

The value of d follows from:

$$d = u_1 - u_0 - t_{AC} \tan\beta = u_1 - u_0 - t_{AC} \frac{u_0}{t_{CB}} \tag{19}$$

After some elaboration follows:

$$d = (u_1 - u_0)\left(1 - \frac{1}{\sin(2\gamma)}\sqrt{\frac{2u_0}{R}}\right) \tag{20}$$

Substituting values, the displacement function $z(t)$ reads:

$$\begin{aligned} z(t) &= \tfrac{1}{2}\sin(2\gamma)\cdot vt \cdot H(t_C - t) + \left(\sqrt{\frac{u_0}{2R}}\cdot vt + d\right)\big(H(t - t_C) - H(t - t_B)\big) + u_1 \cdot H(t - t_B) \\ d &= (u_1 - u_0)\left(1 - \frac{1}{\sin(2\gamma)}\sqrt{\frac{2u_0}{R}}\right) \end{aligned} \tag{21}$$

All parameters can be expressed in the wheel radius R, the rail 'kink' angle γ and the value of u_1 (where instead of u_1 or γ also the length parameter l may be chosen; $\tan\gamma = u_1 / l$). This yields for respectively u_0, β and d (compare Figure 6):

- $u_0 = R - R\cos\gamma = R(1 - \cos\gamma)$ (22)
- $\beta = \sqrt{\tfrac{1}{2}(1 - \cos\gamma)}\cdot v$ or $\beta = \sqrt{\sin^2(\tfrac{1}{2}\gamma)}\cdot v = \sin(\tfrac{1}{2}\gamma)\cdot v$ (23)
- $d = (u_1 - R(1-\cos\gamma))\left(1 - \frac{\sqrt{2(1-\cos\gamma)}}{\sin(2\gamma)}\right) = (u_1 - R(1-\cos\gamma))\underbrace{\left(1 - 2\frac{\sin(\frac{1}{2}\gamma)}{\sin(2\gamma)}\right)}_{\xi}$ (24)

The behaviour of the non-dimensional factor ξ is shown in Figure 8, for $0 < \gamma < 90°$ ($0 < \gamma < \frac{1}{2}\pi$): $-\infty < \xi < \frac{1}{2}$. For small γ, the value 0.5 can be adopted.

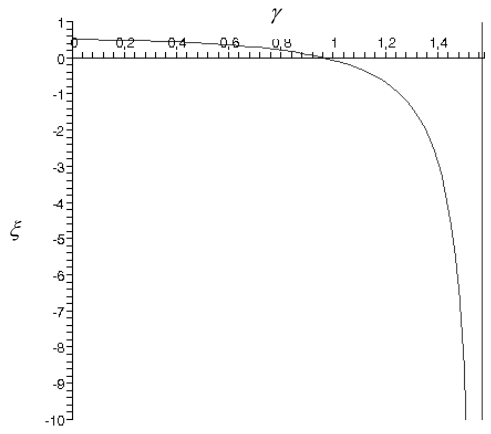

Fig. 8. Behaviour of ξ versus γ for $0 < \gamma < \frac{1}{2}\pi$

Summarising, the total displacement function now reads (with $t_A = 0$, $t_C = t_{AC}$ and $t_B = t_{AC} + t_{CB}$):

$$z(t) = \tfrac{1}{2}\sin(2\gamma)\cdot vt\cdot H(t_C - t) + \left(\sin(\tfrac{1}{2}\gamma)\cdot vt + d\right)\cdot\left(H(t-t_C) - H(t-t_B)\right) + u_1\cdot H(t-t_B) \qquad (25)$$

where

$$d = (u_1 - R(1-\cos\gamma))\left(1 - 2\frac{\sin(\frac{1}{2}\gamma)}{\sin(2\gamma)}\right)$$

$$t_C = \frac{2}{\sin(2\gamma)}\frac{(u_1 - R(1-\cos\gamma))}{v}$$

$$t_B = \frac{2}{\sin(2\gamma)}\frac{(u_1 - R(1-\cos\gamma))}{v} + 2\sin(\tfrac{1}{2}\gamma)\frac{R}{v}$$

Introducing the simplification $\gamma \ll \frac{1}{2}\pi$ (which is a realistic assumption for practice), the expressions can be simplified significantly; the complete formulation of the excitation of the wheel model takes the following form:

$$\dot{u}(0) = \gamma\cdot v \qquad (26)$$

and

$$z(t) = \gamma\cdot vt\cdot H(t_C - t) + \tfrac{1}{2}\left(\gamma\cdot vt - \tfrac{1}{2}\gamma^2 R + u_1\right)\cdot\left(H(t-t_C) - H(t-t_B)\right) + u_1\cdot H(t-t_B)\ \ (t \geq 0) \qquad (27)$$

where

$$t_C = \frac{R}{v}\left(\frac{u_1}{\gamma R} - \tfrac{1}{2}\gamma\right)\ \ (>0)\ \text{ and }\ t_B = \frac{R}{v}\left(\frac{u_1}{\gamma R} + \tfrac{1}{2}\gamma\right)\ \ (>0)$$

with model restrictions: $0 < \gamma \ll 90°$ and $\frac{1}{2}\gamma^2 < u_1/R < 1$.

In Figure 9 an example of the displacement according to equation (27) is shown, for the arbitrary parameter values:

- $\gamma = 18°$
- $R = 0.4$ m
- $u_1 = 0.04$ m (which is a theoretical value, used for clearness of the graph)
- $v = 80$ km/h

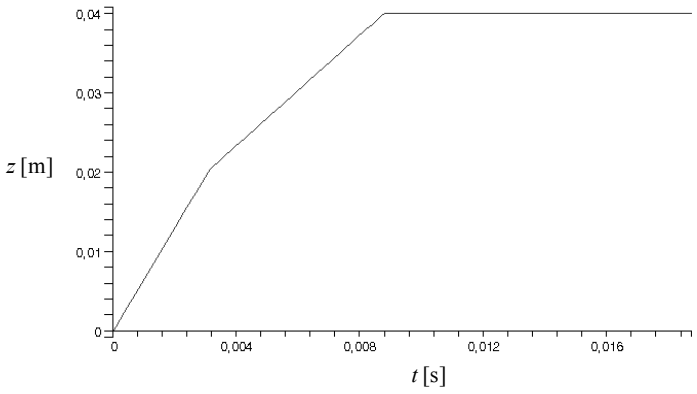

Fig. 9. Example of a piecewise linear displacement function according to equation (27)

5. DISCUSSION

In both cases treated in the previous section, a linearisation of the trajectory was used, for simplicity and transparency of analysis. It is obvious that taking the original, partly circular, displacement will only increase dynamic effects.

The rail profiles as considered in the sections 4.1 and 4.2 only have theoretical meaning, as these profiles will never occur in practice. However, they clearly demonstrate the impact problem for 2-point contact. Further, the multi-linear case very clearly shows the principle of what will occur e.g. in case of a dipped joint: impact followed by a continuous system excitation (Figure 10).

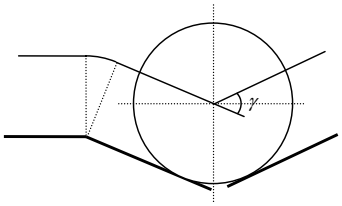

Fig. 10. Wheel centre trajectory with discontinuous derivative at a dipped joint

In general, the impact will be the dominating factor, and the vertical shift in the contact point can be found, for certain wheel radius, from the considered geometry. This vertical shift determines the impact magnitude, which in reality is finite, as will be explained in the following.

In the previous, all derivations were geometrical or kinematical. Both inertia and elasticity were not accounted for. The effect of elasticity is smoothing. In reality the velocity change as well as the impact will not occur in a zero time-interval, but in a finite time-interval. Also the magnitude will not be infinite, but reach only a finite value.

Further, with high impact loads, plasticity will play an important role. Its role is, next to contact stress redistribution, physical smoothing due to plastic deformation (at least for the rail), which will decrease dynamic effects too [7].

Finally, the rail system (the foundation) was considered as completely rigid during impact. As long as the time interval of impact approaches zero this is a correct assumption also for a non-rigid foundation; both wheel and rail inertia prevent them from displacing *during* this time interval. However, when the elasticity of the wheel is taken into account, the duration of impact will not be zero any more, and elasticity of the track will start to play a role. This means that for real track the above is only an approximation for derivation of the relative wheel-rail displacement, which is the best possible with a discrete wheel model.

From the previous it follows that it is not necessarily correct modelling the wheel as a lumped mass on a Hertz spring with excitation possibility only at the base of the spring. As soon as a shift of the contact-point occurs, impact forces may occur, with dynamic effects linearly increasing with the train velocity and with magnitude which may reach much higher values than would occur in the case of continuous single-point-contact, due to the impact character.

This will be illustrated below, again for a rigid foundation, and assuming linear behaviour. In Figure 11 the response (displacement and velocity of the wheel-mass and contact force) is shown of the theoretical wheel-model of Figure 3 passing a step u_0 in a rail on rigid foundation at velocity v for two different cases.

At the left, the system response is shown for the case of an impact load on the wheel-mass. The equation of motion of the system is:

$$m_w \ddot{u}(t) + k_H u(t) = m_w v_0 \delta(t) \tag{28}$$

where δ denotes the Dirac-delta-function; $v_0 = v \cdot \sqrt{2u_0 / R}$ according to equation (2). The solution amplitude reads:

$$\hat{u} = v\sqrt{\frac{2m_w u_0}{k_H R}} \tag{29}$$

and the contact force amplitude equals

$$\hat{F} = v\sqrt{\frac{2u_0 k_H m_w}{R}} \,. \tag{30}$$

The wheel-mass has a zero initial displacement and a non-zero initial velocity; the wheel-rail contact force starts with an infinite peak of zero duration (initial condition), after which it is exactly in phase with the wheel displacement on the Hertz spring.

At the right, the results are shown for a similar model, but assuming continuous single-point-contact, with a step-excitation at the base of the Hertz-spring. The equation of motion of the system is:

$$m_w \ddot{u}(t) + k_H u(t) = k_H u_0 H(t) \tag{31}$$

where H denotes the Heaviside-function. The solution amplitude reads:

$$\hat{u} = 2u_0 \tag{32}$$

and the contact force amplitude:

$$\hat{F} = 2k_H u_0 \tag{33}$$

where the influence of wheel mass and radius, as well as that of the velocity have vanished (which is obviously wrong for a train wheel). Results are different, also as regards the behaviour in time. No impact occurs; displacement of the wheel starts at zero, with zero slope, though the contact force starts at its amplitude, as a result of the instantaneous compression of the Hertz-spring.

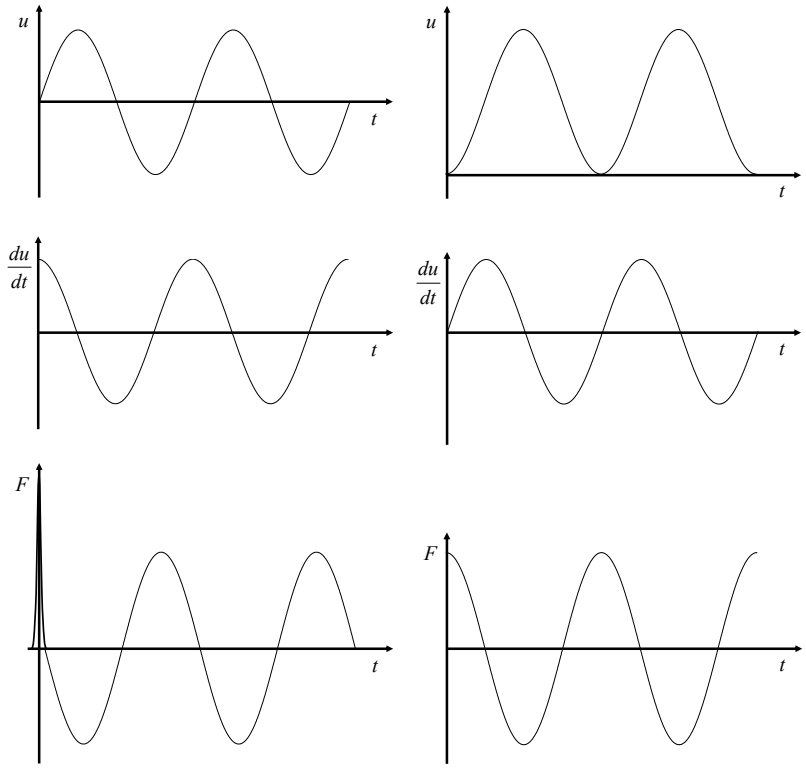

Fig. 11. Qualitative model comparison for a wheel passing a step, assuming double-point-contact with corresponding impact (left) and continuous single-point-contact with corresponding Hertz-spring excitation (right). Shown is the displacement of the mass, its velocity, and the contact-force in the Hertzian spring.

6. APPLICATION TO A CONTINUOUSLY EMBEDDED RAIL-WHEEL SYSTEM

The above now will be applied to a vertical wheel-rail interaction model. A simple, linear model is chosen, so that analytical solutions can be obtained. The train vehicle is modelled up to the level of the primary suspension. Physical as well as geometrical linearity is assumed. This strongly reduces the practical applicability of the model, but enables an approach in the frequency domain. The moving oscillator problem may be simplified to a standing oscillator problem (where the rail irregularity moves with speed v between rail and spring base) because of the fact that the wave propagation and reflection at the irregularity in the system due to the moving oscillator itself is not of interest here and will have negligible effects on contact forces at the discontinuity. The model is shown in Figure 12, where also some notations are introduced.

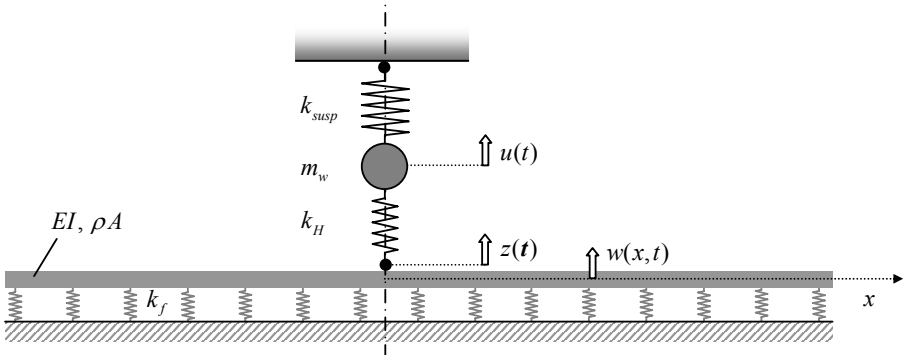

Fig. 12. Wheel-rail interaction model with excitation $z(t)$

The following mathematical statement of the problem is valid:

- Beam (Euler-Bernoulli) on elastic foundation:

$$EI\frac{\partial^4 w(x,t)}{\partial x^4}+\rho A\frac{\partial^2 w(x,t)}{\partial t^2}+k_f w(x,t)=-F(t)\delta(x) \tag{34}$$

- Oscillator:

$$m_w\frac{d^2u(t)}{dt^2}+k_{susp}u(t)=F(t) \tag{35}$$

- Contact force:

$$F(t)=k_H\left(-u(t)+w(0,t)+z(t)\right) \tag{36}$$

- Boundary conditions: no perturbations at $-\infty$ and $+\infty$
- Initial conditions assumed zero, except for the initial velocity of the wheel mass and the rail contact point, which is assumed $\dot{u}(0)=v_0$ and $\dot{w}(0,0)$ respectively.

The functions $z(t)$ for different weld geometries have been derived in the previous sections.

7. SOLUTION IN THE FREQUENCY DOMAIN

The problem (34-36) will be solved applying integral transform methods. The governing equation (34) of the beam in the *t,x* domain is written as:

$$\frac{\tilde{\partial}^4 w(x,t)}{\partial x^4}+\frac{1}{a^2}\frac{\tilde{\partial}^2 w(x,t)}{\partial t^2}+b^2 w(x,t)=-\frac{1}{EI}F(t)\delta(x) \text{ with } a=\sqrt{\frac{EI}{\rho A}},\ b=\sqrt{\frac{k_f}{EI}} \tag{37}$$

Laplace-transforming this equation with respect to time, with initial displacement assumed zero and arbitrary initial velocity $\dot{w}(x,0)$, yields:

$$\frac{\tilde{\partial}^4 \tilde{w}(x,s)}{\partial x^4} + \left(\frac{s^2 - \dot{w}(x,0)}{a^2} + b^2 \right) \tilde{w}(x,s) = -\frac{1}{EI} \tilde{F}(s) \delta(x) \tag{38}$$

where the transformed variable is indicated by a tilde. The general solution to the homogeneous problem is of the form:

$$\tilde{w} = C_1 e^{px} + C_2 e^{-px} + C_3 e^{ipx} + C_4 e^{-ipx} \tag{39}$$

where $p = \frac{1}{\sqrt{2}} (1+i) \sqrt[4]{\frac{s^2 - \dot{w}(x,0)}{a^2} + b^2}$

Normally, the constants C can be determined applying the boundary conditions. However, since the beam is undisturbed at both $-\infty$ and $+\infty$, it can be concluded immediately that all constants are equal to zero, and thus that the homogeneous solution vanishes.

For the inhomogeneous problem, the particular solution to the right-hand-side must be added, denoted by $\tilde{w}_{\text{part}}$. It will be determined applying a Fourier transform on the governing equation with respect to x. The Fourier transformed governing equation reads:

$$\bar{\tilde{w}}(k,s) \left(k^4 + \frac{s^2 - \dot{w}(x,0)}{a^2} + b^2 \right) = -\frac{1}{EI} \tilde{F}(s) \tag{40}$$

where the Fourier-transformed variable has been indicated by a bar. This yields for the particular solution:

$$\bar{\tilde{w}} = -\frac{1}{EI} \frac{\tilde{F}(s)}{k^4 + \frac{s^2 - \dot{w}(x,0)}{a^2} + b^2} \tag{41}$$

The inverse Fourier transform of this solution yields the particular solution in the x,s domain:

$$\tilde{w}_{\text{part}}(x,s) = -\frac{\tilde{F}(s)}{2\pi EI} \int_{-\infty}^{\infty} \frac{e^{-ikx}}{k^4 + \frac{s^2 - \dot{w}(x,0)}{a^2} + b^2} dk \tag{42}$$

The integral can be calculated by contour integration, adding a semicircle joining $-\infty$ to ∞ and applying respectively Jordan's lemma and Cauchy's residue theorem. This derivation is carried out in Appendix A. The result of the integration reads for all x:

$$\int_{-\infty}^{\infty} \frac{e^{-ikx}}{k^4 + \frac{s^2 - \dot{w}(x,0)}{a^2} + b^2} dk = \frac{\pi}{8k_0^3} \left((1-i) e^{(-1+i)k_0|x|} + (1+i) e^{(-1-i)k_0|x|} \right) \tag{43}$$

Substitution of equation (43) into (42) yields the particular solution in the *s*,*x* domain for the load, which also represents the total solution:

$$\tilde{w}(x,s) = -\frac{\tilde{F}(s)}{16EIk_0^3}\left((1-i)e^{(-1+i)k_0|x|} + (1+i)e^{(-1-i)k_0|x|}\right) \tag{44}$$

where

$$k_0 = \frac{1}{\sqrt{2}}\sqrt[4]{\frac{s^2 - \dot{w}(x,0)}{a^2} + b^2}\ ,\ s = \sigma + i\omega$$

Now attention will be turned to the oscillator, the wheel mass. The equation of motion (35), Laplace-transformed with respect to time, reads (again assuming zero initial displacement, but a non-zero initial velocity v_0 and denoting the transformed variable by a tilde):

$$-m_w\dot{u}(0) + \left(m_w s^2 + k_{susp}\right)\tilde{u}(s) = \tilde{F}(s) \tag{45}$$

From this follows directly:

$$\tilde{u}(s) = \frac{\tilde{F}(s) + m_w v_0}{m_w s^2 + k_{susp}} \tag{46}$$

The coupling between (44) and (46) is established by means of the contact force (36). This expression, Laplace-transformed with respect to time, reads:

$$\tilde{F}(s) = k_H\left(-\tilde{u}(s) + \tilde{w}(0,s) + \tilde{z}(s)\right) \tag{47}$$

Substitution of the expressions (44) for $\tilde{w}(x,s)$ and (46) for $\tilde{u}(s)$ yields, after some elaboration, the final expression for the contact force $\tilde{F}(s)$ in the Laplace-domain:

$$\tilde{F}(s) = \frac{\tilde{z}(s) - \dfrac{m_w v_0}{m_w s^2 + k_{susp}}}{\dfrac{1}{k_H} + \dfrac{1}{m_w s^2 + k_{susp}} + \dfrac{1}{8EIk_0^3}} \tag{48}$$

where $k_0 = \dfrac{1}{\sqrt{2}}\sqrt[4]{\dfrac{s^2 - \dot{w}(0,0)}{a^2} + b^2}$ and $s = \sigma + i\omega$; $a = \sqrt{\dfrac{EI}{\rho A}}$ and $b = \sqrt{\dfrac{k_f}{EI}}$.

The input for v_0 has been determined in section 4, equations (2) and (26). The input for $\dot{w}(0,0)$ will be determined in the following. As seen, the wheel gets an initial upward velocity at the moment of impact. The rail at this moment gets the same initial velocity, but in downward direction, or: $\dot{w}(0,0) = -v_0$. This can be

explained as follows. At the moment of impact, when the wheel rim hits the rail, the rail cross-section in question, which in theory has *zero* mass as its length is infinitely small, gets a certain initial velocity. Assuming a purely elastic impact, the value of this velocity should be the same as the value of the wheel initial vertical velocity, as displacements are zero. After impact, or for $t > 0$, wave propagation from the impact coordinate occurs, introducing non-zero deflections and velocities (and thus momentum) in other cross-sections of the beam.

The expressions for $z(t)$ also have been determined in section 4, but still must be transformed to the frequency domain. The Laplace-transformed functions $z(t)$ (8) and (27) can be found relatively easy and read, for both respective cases:

$$\tilde{z}(s) = \sqrt{\frac{u_0}{2R}} \cdot \frac{v}{s^2}\left(1 - e^{-\sqrt{2Ru_0}\cdot s/v}\right) \tag{49}$$

and

$$\tilde{z}(s) = \frac{1}{s}\left[\gamma \cdot v \cdot \frac{e^{-t_C s}}{s}\left(e^{t_C s} - 1 - t_C s\right) + \tfrac{1}{2}\gamma \cdot v \cdot \frac{1}{s}\left(e^{-t_C s}\left(t_C s + 1\right) - e^{-t_B s}\left(t_B s + 1\right)\right) + \left(\tfrac{1}{2}u_1 - \tfrac{1}{4}\gamma^2 R\right)\left(e^{-t_C s} - e^{-t_B s}\right) + u_1 e^{-t_B s}\right] \tag{50}$$

with t_C and t_B as defined in (27).

In Figure 13 the spectrum of the displacement according to equation (50) is given for the same parameter values as have been used in Figure 8. The symmetry of the real part and antimetry of the imaginary part are obvious. The function rapidly decays with increasing frequency (or *s*), as is necessary for convergence of the integration process.

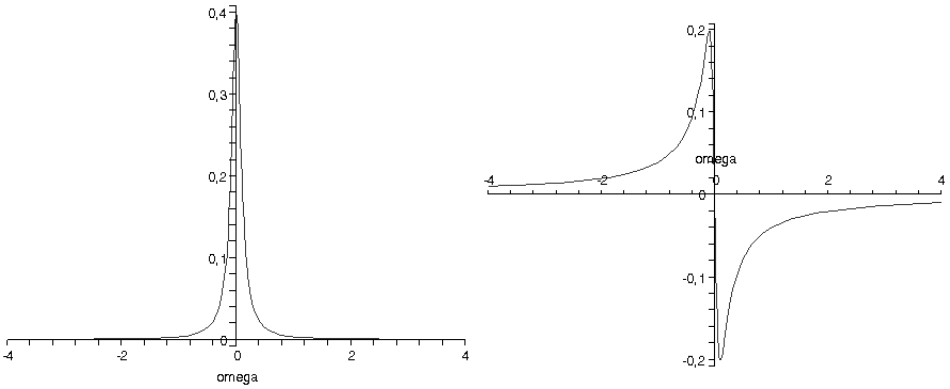

Fig. 13. Real and imaginary part of the transformed excitation $\tilde{z}(s)$ versus ω ($s = \sigma + i\omega$; $\sigma = 0.1$)

8. PARAMETRICAL AND NUMERICAL SOLUTIONS IN THE TIME DOMAIN

The expression (48) must be inversely transformed to the time domain. This inverse transform (integration over the frequency) will be carried out numerically as the analytical transform by means of contour integration implies the complex branch cutting. The numerical procedure is explained in Appendix B. The result is that the inverse Laplace-transform of $\tilde{F}(s)$ can be written as:

$$F(t) = \frac{e^{\sigma t}}{\pi} \int_0^\infty \mathrm{Re}\left(\tilde{F}(s)\right) e^{i\omega t} d\omega \tag{51}$$

This expression can be used for numerical integration of the solution in the Laplace domain. The general expression, in integral form, for the dynamic contact force wheel-rail as a function of time, for an arbitrary excitation function $z(t)$ with Laplace-image $\tilde{z}(s)$ reads:

$$F(t) = \frac{e^{\sigma t}}{\pi} \int_0^\infty \mathrm{Re}\left(\frac{\tilde{z}(s) - \dfrac{m_w v_0}{m_w s^2 + k_{susp}}}{\dfrac{1}{k_H} + \dfrac{1}{m_w s^2 + k_{susp}} + \dfrac{1}{8EIk_0^3}} \right) e^{i\omega t} d\omega \tag{52}$$

where $k_0 = \dfrac{1}{\sqrt{2}} \sqrt[4]{\dfrac{s^2 + v_0}{a^2} + b^2}$, $a = \sqrt{\dfrac{EI}{\rho A}}$, $b = \sqrt{\dfrac{k_f}{EI}}$ and $s = \sigma + i\omega$.

The value of v_0 is zero for continuous single-point-contact; for two special cases of double-point-contact the values have been determined in equations (2) and (26).

In the following some numerical evaluations of expression (52) will be made. First, numerical values will be adopted for the parameters playing a role. In Table 1 some material and geometrical properties for both track and vehicle are specified. Data have been taken from [2] and mainly from [13].

Table 1. Physical properties of vehicle and track components

Young's modulus of steel E	$2.1 \cdot 10^{11}$ N/m^2
Poisson's ratio of steel υ	0.3
Steel density ρ	7850 kg/m^3
Railhead radius R_{rail} (UIC)	0.3 m
Rail cross-sectional area A (UIC54)	$6930 \cdot 10^{-6}$ m^2
Rail moment of inertia I (UIC 54)	$2346 \cdot 10^{-8}$ m^4
Rail foundation stiffness k_f	$48 \cdot 10^6$ N/m^2
Train wheel radius R	0.46 m
Train wheel mass m_w (locomotion)	2000 kg

Stiffness primary suspension k_{susp} (locomotion)	$2.25 \cdot 10^6$ N/m
Vertical static wheel-load Q (locomotion)	$112.5 \cdot 10^3$ N
Train velocity v	22.2 m/s (80 km/h)

The considered rail irregularities are defined by $\gamma = 0.01$ rad, $u_1 = 0.0025$ m and $u_0 = 0.001$ m respectively, compare Figure 14.

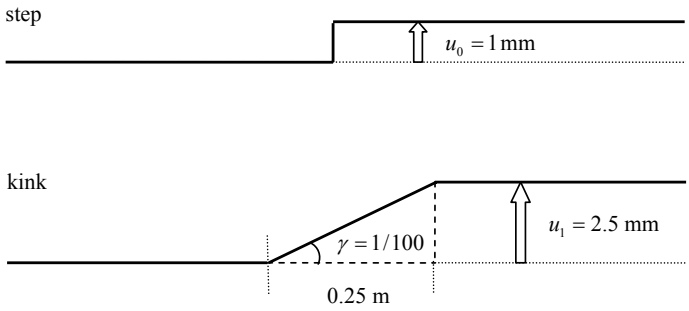

Fig. 14. Considered rail irregularities and their definition

The contact stiffness wheel-rail due to elastic deformations of the wheel-body and the rail surface can be derived from the Hertz contact theory. Here the simplified expression from [2] will be used, which reads:

$$k_H = \sqrt[3]{\frac{3E^2 Q\sqrt{R \cdot R_{rail}}}{2\left(1-\upsilon^2\right)^2}} \tag{53}$$

Substituting material and geometrical properties from Table 1, the following expression ensues:

$$k_H = \sqrt[3]{3 \cdot 10^{22} Q} \tag{54}$$

Calculation results for the step (Figure 14) are shown in the graphs of Figure 15, at the left zoomed in for short time duration and at the right for longer time duration (steady-state response).

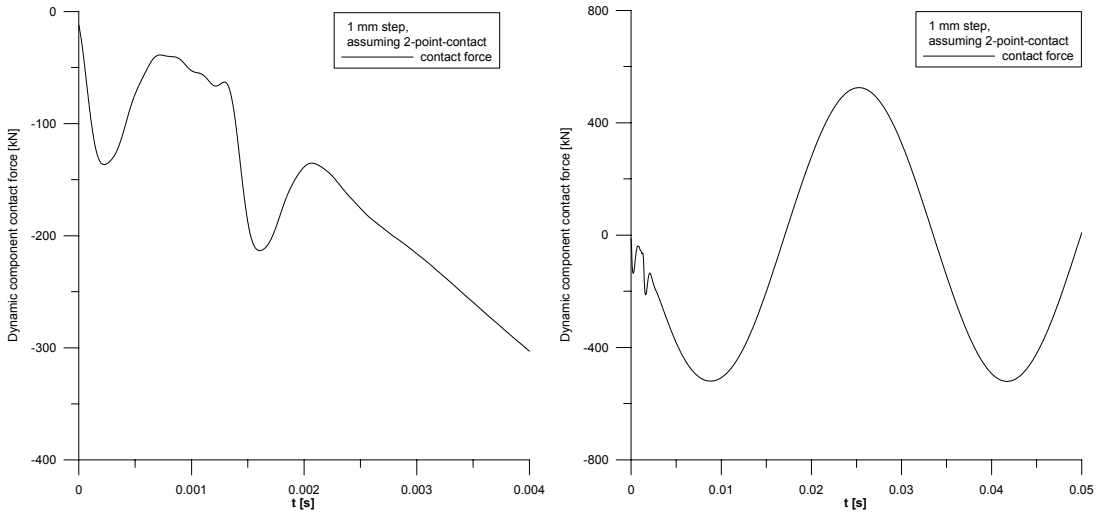

Fig. 15. Model response (contact force wheel-rail) after impact for short (left) and longer (right) time duration; step excitation

It should be noticed that the first peak in the contact force (the impact force itself) is not calculated, as it is used as a discrete initial condition; only the response after impact is shown. The contact force starts at zero, with certain slope, due to the initial velocity of the wheel-mass. The oscillation is disturbed by the further system excitation given by equation (8), which ends at $t = 0.0014$ s (Equation (7)), when the wheel has 'climbed' the step. High frequencies (with the highest frequency in the response spectrum determined by the natural frequency of the wheel mass on the Hertz spring) travel away in the rail from the contact point with the highest velocity. Very quickly, the system comes in a sort of overall natural frequency, corresponding to the so-called trapped mode, where also the equivalent track mass, foundation stiffness and primary suspension play a role. The frequency corresponding to the trapped mode (which is estimated as 190 rad/s) should be smaller than the cut-off frequency of the beam, which can be verified easily. The cut-off frequency of the rail can be found from the stiffness of the foundation and the distributed mass of the rail per unit of length and equals 940 rad/s. However, at this lower frequency also the bogie mass starts to play a role, which was not incorporated in the model. The static wheel-load was taken as 112.5 kN, where in Figure 15 negative contact forces larger than 500 kN occur. This means non-linearities (loss of contact) will play an important role: in reality the wheel will start bouncing on the rail after impact.

In Figure 16 the system response is shown again for the step excitation of Figure 14, but now *assuming continuous single-point contact*. Thus, the Hertzian spring base passes the step and no impact occurs; $v_0 = 0$.

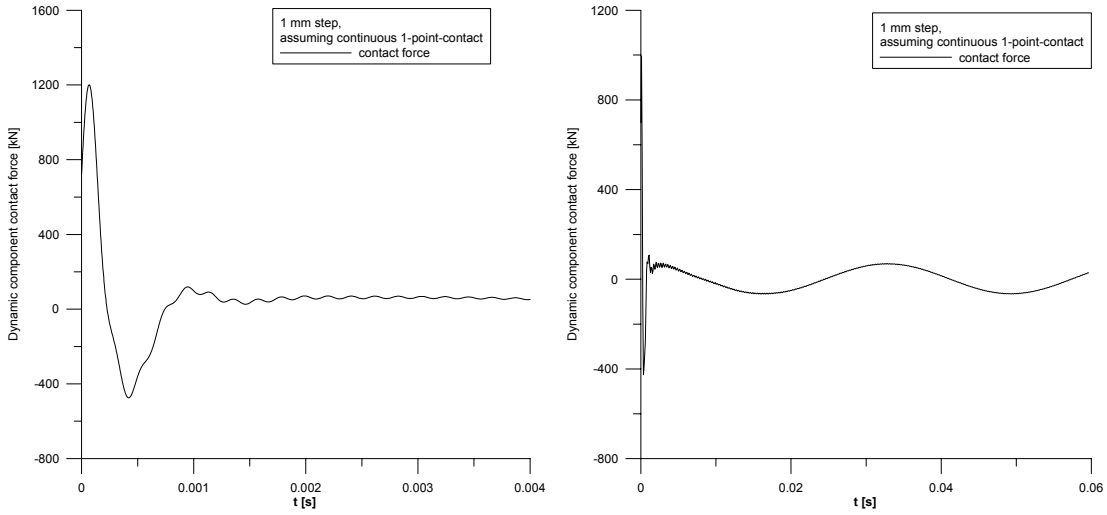

Fig. 16. Wheel-rail contact force for a step excitation, *assuming 1-point-contact*, for short (left) and longer (right) time duration

The response has a behaviour in time which is completely different from the behaviour as found with two-point-contact. The contact force starts with a large positive value, due to the instantaneous compression of the Hertz spring. Afterwards, again the system ends up in the trapped mode, which is even clearer than in Figure 15. Comparison of the results of Figure 15 and 16 with the results from Figure 11, for rigid track, shows that results are basically similar.

In Figure 17, calculation results are given for the kinked rail geometry, as shown in Figure 14.

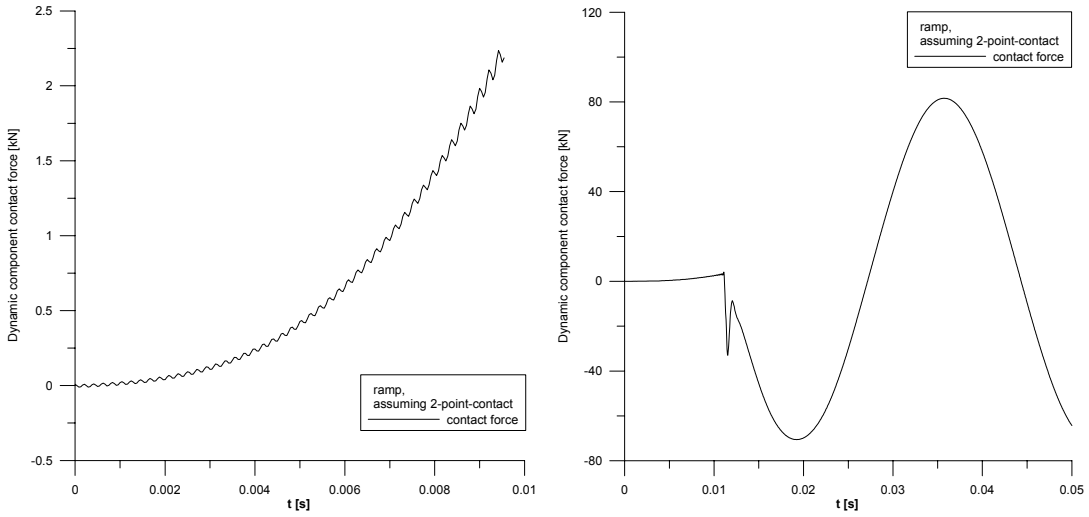

Fig. 17. Model response (contact force wheel-rail) after impact for a kinked rail geometry, for short (left) and longer (right) time duration

Basically, the same happens as for the step. However, a strange effect occurs due to on the one hand the response to the initial impact, and at the other hand the response to the system excitation as the wheel 'climbs'

the ramp: they cancel each other more or less. The system excitation stops at $t_C = 0.011\,\mathrm{s}$ (Equation (27)), which is clearly visible in Figure 17. Again, the system ends in the trapped mode. As the static preload equals 112.5 kN, no loss of contact will occur *after* impact.

9. CONCLUDING REMARKS

The applicability of lumped wheel models has been studied for situations where two- or more-point-contact between wheel and rail can occur, like dipped rail joints. It has been shown that in principle application of these models cannot describe occurring mechanisms fully correct. The assumption of continuous single-point contact (as is made using a model of a lumped mass on a Hertz spring) automatically excludes the possibility of impact, as this is caused by a discontinuity in the single-point contact. The problem can be avoided applying an instantaneous vertical velocity change to the wheel mass, with magnitude following from the vertical rail geometry and the wheel radius. However, in this way a singularity in the contact-force occurs, which goes to infinity in a zero time duration. In reality this effect is smoothed, but the best possible approximation of what occurs in reality is obtained for a lumped wheel model.

For practice, it is important to avoid short-length rail irregularities where two-point-contact can occur. As regards the high impact loads, they are not only caused by geometrical discontinuities, but also by short-length irregularities where non-linear dynamic behaviour (hammering, or single-point-contact which is discontinuous in time) occurs. Short wavelengths or high frequencies are detrimental to the track; one think of e.g. concrete sleepers. Most critical are those wavelengths that are just beyond the limit of plastification. The plastification limit, and thus the critical wavelength, depends, apart from material properties, mainly on the axle loads and the running speeds. In addition, loss of contact wheel-rail will cause rapid wear of both rail and wheel, as the wheel is not a static element, but running. This wear will not be continuous in longitudinal direction of the rail, but cause even a deterioration of the vertical rail geometry in longitudinal direction.

As rail joints, even in CWR-track, are the most critical elements as regards the vertical rail geometry, it is important to realize joint-geometries with as small vertical tolerances as possible. In this way, numerous well-known and cost-intensive problems like rolling contact fatigue (RCF), corrugation and rapid wear [14] can be avoided.

Appendix A

The poles of the integrand (42) are equal to the solutions of the equation

$$k^4 + \frac{s^2 - \dot{w}(x,0)}{a^2} + b^2 = 0 \quad \Rightarrow \quad k_{1,2,3,4} = \frac{1}{\sqrt{2}}(\pm 1 \pm i)\sqrt[4]{\frac{s^2 - \dot{w}(x,0)}{a^2} + b^2} \tag{55}$$

or

$$k_1 = (1+i)k_0;\ k_2 = (-1-i)k_0;\ k_3 = (1-i)k_0;\ k_4 = (-1+i)k_0 \tag{56}$$

where

$$k_0 = \frac{1}{\sqrt{2}}\sqrt[4]{\frac{s^2 - \dot{w}(x,0)}{a^2} + b^2} \tag{57}$$

The behaviour of the imaginary part of the poles is shown in Figure 18, where the definition of the Laplace parameter s has been used, $s = \sigma + i\omega$ with $\sigma > 0$.

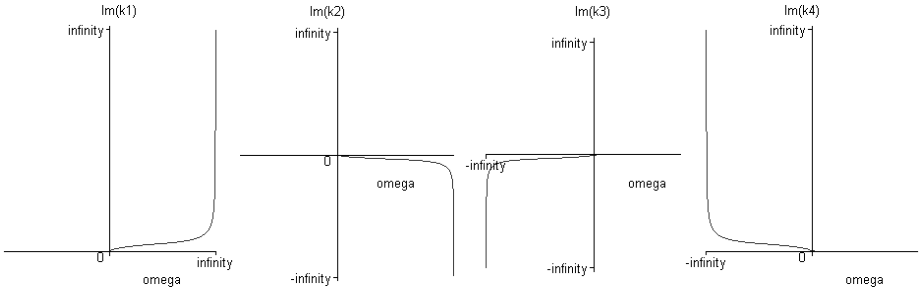

Fig. 18. Behaviour of the imaginary parts of the poles versus ω (for small $\sigma > 0$)

It can be concluded: $\mathrm{Im}(k_1) > 0,\ \mathrm{Im}(k_2) < 0,\ \mathrm{Im}(k_3) < 0,\ \mathrm{Im}(k_4) > 0$, from which is known which poles lay in the upper half-plane (k_1 and k_4) and which ones in the lower half-plane (k_2 and k_3) of the complex plane. According to Jordan's lemma the contour should be closed in the upper half-plane in the case $x < 0$ and in the lower half-plane in the case $x > 0$. Both closed contours and the poles are shown in Figure 19.

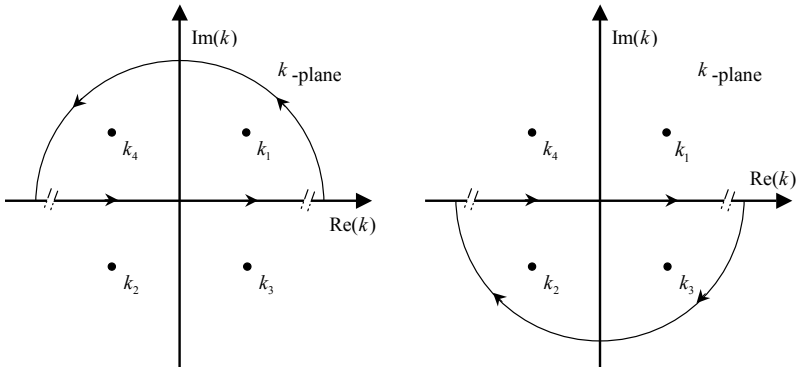

Fig. 19. Closed contours for $x<0$ respectively $x>0$

As the integrand is single-valued, Cauchy's residue theorem can be applied now. First it will be applied for the first contour, $x<0$. Inside the contour are two poles. The residue theorem states:

$$\int_{-\infty}^{\infty} \frac{e^{-ikx}}{k^4+\frac{s^2-\dot{w}(x,0)}{a^2}+b^2}dk = 2\pi i \sum_{k_1,k_4} Residue\ of\ \frac{e^{-ikx}}{k^4+\frac{s^2-\dot{w}(x,0)}{a^2}+b^2}\ at\ k_{1,4} = 2\pi i \sum_{k_1,k_4} \left.\frac{e^{-ikx}}{4k^3}\right|_{k_{1,4}} \tag{58}$$

Evaluating this expression, with the poles defined by (57), yields:

$$\int_{-\infty}^{\infty} \frac{e^{-ikx}}{k^4+\frac{s^2-\dot{w}(x,0)}{a^2}+b^2}dk = 2\pi i \sum_{k_1,k_4} \left.\frac{e^{-ikx)}}{4k^3}\right|_{k_{1,4}} = 2\pi i\left(\frac{e^{-i(1+i)k_0x}}{4\left((1+i)k_0\right)^3}+\frac{e^{-i(-1+i)k_0x}}{4\left((-1+i)k_0\right)^3}\right)$$

$$=\frac{\pi}{8k_0^3}e^{k_0x}\left((1-i)e^{-ik_0x}+(1+i)e^{ik_0x}\right)$$

Since $x<0$, this result can be written as:

$$\frac{\pi}{8k_0^3}\left((1-i)e^{(-1+i)k_0|x|}+(1+i)e^{(-1-i)k_0|x|}\right) \tag{59}$$

In an analogous way follows for the 2nd contour (which is in the negative sense; a minus should be added), $x>0$:

$$\int_{-\infty}^{\infty} \frac{e^{-ikx}}{k^4+\frac{s^2-\dot{w}(x,0)}{a^2}+b^2}dk = -2\pi i \sum_{k_2,k_3} \left.\frac{e^{-ikx}}{4k^3}\right|_{k_{2,3}} = -2\pi i\left(\frac{e^{-i(-1-i)k_0x}}{4\left((-1-i)k_0\right)^3}+\frac{e^{-i(1-i)k_0x}}{4\left((1-i)k_0\right)^3}\right)$$

$$=\frac{\pi}{8k_0^3}\left((1-i)e^{(-1+i)k_0x}+(1+i)e^{(-1-i)k_0x}\right)$$

This may be written as ($x>0$):

$$\frac{\pi}{8k_0^3}\left((1-i)e^{(-1+i)k_0|x|}+(1+i)e^{(-1-i)k_0|x|}\right) \tag{60}$$

which is exactly the same result as found above (expression (59)) for the first contour. Thus, the integral can be evaluated for all *x* as (for $x=0$ the contour may be closed anyhow):

$$\int_{-\infty}^{\infty}\frac{e^{-ikx}}{k^4+\dfrac{s^2-\dot{w}(x,0)}{a^2}+b^2}dk=\frac{\pi}{8k_0^3}\left((1-i)e^{(-1+i)k_0|x|}+(1+i)e^{(-1-i)k_0|x|}\right) \tag{61}$$

Appendix B

The inverse Laplace-transform of $\tilde{F}(s)$ is defined as:

$$F(t)=\frac{1}{2\pi i}\int_{\sigma-i\infty}^{\sigma+i\infty}\tilde{F}(s)e^{st}ds \tag{62}$$

Substituting $s=\sigma+i\omega$ with σ some small positive value, or $ds=id\omega$, and $-\infty<\omega<\infty$, yields:

$$F(t)=\frac{e^{\sigma t}}{2\pi}\int_{-\infty}^{\infty}\tilde{F}(\sigma+i\omega)e^{i\omega t}d\omega$$

The integrand in this expression can be elaborated as follows:

$$\tilde{F}\cdot e^{i\omega t}=\left(\mathrm{Re}(\tilde{F})+i\,\mathrm{Im}(\tilde{F})\right)\cdot\left(\cos\omega t+i\sin\omega t\right)=\underbrace{\mathrm{Re}(\tilde{F})\cos\omega t-\mathrm{Im}(\tilde{F})\sin\omega t}_{\text{Real part}}+\underbrace{i\left(\mathrm{Re}(\tilde{F})\sin\omega t+\mathrm{Im}(\tilde{F})\cos\omega t\right)}_{\text{Imaginary part}}$$

where the imaginary part of the integrand should add up to 0, as the force $F(t)$ is real. This means, $\sin\omega t$ being anti-symmetric and $\cos\omega t$ symmetric with respect to ω, that $\mathrm{Re}(\tilde{F})$ is a symmetric and $\mathrm{Im}(\tilde{F})$ an anti-symmetric function of ω. Thus for the integral may be written:

$$F(t)=\frac{e^{\sigma t}}{2\pi}\int_{-\infty}^{\infty}\mathrm{Re}\left(\tilde{F}(s)\right)e^{i\omega t}d\omega=\frac{e^{\sigma t}}{\pi}\int_{0}^{\infty}\mathrm{Re}\left(\tilde{F}(s)\right)e^{i\omega t}d\omega \tag{63}$$

REFERENCES

1. Jenkins, H.H., Stephenson, J, Clayton, G.A., Morland, G.W. and Lyon, D.: The Effect of Track and Vehicle Parameters on Wheel/Rail Vertical Dynamic Forces. *Railway Engineering Journal*, January 1974, pp. 2-16.
2. Esveld, C: *Modern Railway Track*, MRT productions, Zaltbommel, The Netherlands, 2001.
3. ADAMS/Rail, Help Guide, 2002. Available online at: www.mscsoftware.com/products (accessed 23-02-2005).
4. Andersson, C. and Dahlberg, T.: Wheel/rail impacts at a railway turnout crossing. *Proc. Instn. Mech. Engrs, Part F: J. Rail and Rapid Transit* 212 (1998), pp. 123-134.

5. Dukkipati, R.V. and Dong, R.: The Dynamic Effects of Conventional Freight Car Running over a Dipped-joint. *Vehicle System Dynamics* 31 (1999), pp.95-111.

6. Chen, Y.C. and Kuang, J.H.: Contact stress variations near the insulated rail joints. *Proc. Instn. Mech. Engrs, Part F: J. Rail and Rapid Transit* 216 (2002), pp. 265-273.

7. Chen, Y.C.: The effect of proximity of a rail end in elastic-plastic contact between a wheel and a rail. *Proc. Instn. Mech. Engrs, Part F: J. Rail and Rapid Transit* 217 (2003), pp. 189-201.

8. Wu, T.X. and Thompson, D.J.: On the impact noise generation due to a wheel passing over rail joints. *Journal of Sound and Vibration* 267 (2003), pp.485-496.

9. Wu, T.X. and Thompson, D.J.: The effects of track non-linearity on wheel-rail impact. *Proc. Instn. Mech. Engrs, Part F: J. Rail and Rapid Transit* 218 (2004), pp. 1-10.

10. Schupp, G., Weidemann, C. and Mauer, L.: Modelling the Contact Between Wheel and Rail Within Multibody System Simulation. *Vehicle System Dynamics* 41 (2004), pp.349-364.

11. Koro, K., Abe, K., Ishida, M. and Suzuki, T.: Timoshenko beam finite element for vehicle-track vibration analysis and its application to jointed railway track. *Proc. Instn. Mech. Engrs, Part F: J. Rail and Rapid Transit* 218 (2004), pp. 159-172.

12. Kataoka, H., Abe N., Wakatsuki, O. and Oikawa, Y.: A dynamic stress analysis of joint rails using finite beam element model (in Japanese). In: *Proceedings of the 14th Japan National Symposium on Boundary Element Methods*, 1997, pp. 93-98.

13. De Man, A.P.: *Dynatrack, a survey of dynamic railway track properties and their quality*. Thesis, Delft, Delft University of Technology, The Netherlands, 2002.

14. Popp, K. and Schiehlen, W.: *System Dynamics and Long-Term Behaviour of Railway Vehicles, Track and Subgrade*. Springer Verlag, Berlin, Heidelberg, New York, 2003. (pp. 51-62, Rolling-Contact-Fatigue and Wear of Rails: Economic and Technical Aspects, by Peter Pointner).